Matter and Radiation at Extremes

RESEARCH ARTICLE

pubs.aip.org/aip/mre

The acceleration of a high-charge electron bunch to 10 GeV in a 10-cm nanoparticle-assisted wakefield accelerator

Cite as: Matter Radiat. Extremes 9, 014001 (2024); doi: 10.1063/5.0161687
Submitted: 11 June 2023 • Accepted: 22 October 2023 •
Published Online: 15 November 2023

Constantin Aniculaesei,[1,a] Thanh Ha,[1] Samuel Yoffe,[2] Lance Labun,[1,3] Stephen Milton,[3] Edward McCary,[1] Michael M. Spinks,[1] Hernan J. Quevedo,[1] Ou Z. Labun,[1] Ritwik Sain,[1] Andrea Hannasch,[1] Rafal Zgadzaj,[1] Isabella Pagano,[1,4] Jose A. Franco-Altamirano,[1] Martin L. Ringuette,[1] Erhart Gaul,[1] Scott V. Luedtke,[5] Ganesh Tiwari,[6] Bernhard Ersfeld,[2] Enrico Brunetti,[2] Hartmut Ruhl,[7] Todd Ditmire,[1] Sandra Bruce,[1] Michael E. Donovan,[3] Michael C. Downer,[1] Dino A. Jaroszynski,[2] and Bjorn Manuel Hegelich[1,3,b]

AFFILIATIONS

[1] University of Texas at Austin, Austin, Texas 78712, USA
[2] SUPA Department of Physics, University of Strathclyde, Glasgow, Scotland G4 0NG, United Kingdom
[3] Tau Systems, Inc., Austin, Texas 78701, USA
[4] Lawrence Livermore National Laboratory, Livermore, California 94550, USA
[5] Los Alamos National Laboratory, Los Alamos, New Mexico 87545, USA
[6] Brookhaven National Laboratory, Upton, New York 11973, USA
[7] Ludwig-Maximilians-Universität, Munich, Germany

[a] **Author to whom correspondence should be addressed:** 10gevlab@gmail.com
[b] **Email:** hegelich@physics.utexas.edu

ABSTRACT

An intense laser pulse focused onto a plasma can excite nonlinear plasma waves. Under appropriate conditions, electrons from the background plasma are trapped in the plasma wave and accelerated to ultra-relativistic velocities. This scheme is called a laser wakefield accelerator. In this work, we present results from a laser wakefield acceleration experiment using a petawatt-class laser to excite the wakefields as well as nanoparticles to assist the injection of electrons into the accelerating phase of the wakefields. We find that a 10-cm-long, nanoparticle-assisted laser wakefield accelerator can generate 340 pC, 10 ± 1.86 GeV electron bunches with a 3.4 GeV rms convolved energy spread and a 0.9 mrad rms divergence. It can also produce bunches with lower energies in the 4–6 GeV range.

I. INTRODUCTION

Since Tajima and Dawson's initial proposal of the concept in 1979,[1] the concept of laser wakefield acceleration (LWFA) has been considered promising for the shrinking of kilometer-scale conventional accelerators and radiation sources down to room-size machines. A LWFA utilizes a focused short-pulse laser passing through a low-density gas. The laser ionizes the gas and the laser ponderomotive force, which is proportional to the laser intensity gradient, diverts the plasma electrons around the highest intensity regions of the laser pulse, producing nonlinear plasma waves (NPW).[2] The plasma electrons form a dense sheath around the quasi-stationary ions and create what has been called the "bubble"[3] or "blowout"[4] regime. The trajectories of the sheath electrons collapse radially back onto themselves at the back of the bubble. The large space-charge force then pushes some of these electrons forward into the NPW, where they can be accelerated to relativistic velocities by strong acceleration gradients. The LWFA acceleration gradients

are roughly three orders of magnitude higher than those obtained using conventional radio-frequency accelerator technology, which explains the great interest in this field of research.

Experiments exploiting the LWFA concept began in the late 1990s[5,6] when chirped pulse amplification[7] using Ti:Sapphire lasers[8] was used to produce intense terawatt-class femtosecond laser pulses.[9] The first quasi-monoenergetic electron bunches from an LWFA,[10,11] produced in 2004, paved the way for the generation of high-quality[12,13] and high energy[14–16] electron bunches from these compact lasers.

Due to the nonlinearity of the LWFA process, the injection position and the number of electrons injected into the wakefield depend very strongly on the laser and gas conditions before the interaction. In an LWFA, shot-to-shot beam stability is a serious challenge. Stable electron accelerator performance is a key requirement for the development of viable applications. Small variations in the laser and gas conditions can lead to shot-to-shot fluctuations of the accelerated electron beam properties. Various schemes have been developed to address and control the stability of LWFAs, including ionization injection,[17] which increases the charge; fast down-ramp injection,[18] which reduces the energy spread and controls the electron energy; and colliding laser beams,[19] which control the electron beam energy. The advantages and disadvantages of each scheme will not be discussed here as they are beyond the scope of this work.

As the injection process seems to be the largest source of beam fluctuations, in the present work, we experimentally explore an alternative method to inject electrons into the NPW using nanoparticles. The use of nanowires and nanoparticles has been shown theoretically[20,21] and experimentally[22] to trigger the injection of electrons into the NPW and increase the charge density, thus providing another possible method for controlling the parameters of the accelerated electron beam. In our experiment, the nanoparticles are generated inside a gas cell through laser ablation of a metal surface and are assumed to be mixed uniformly with the helium gas fed into the gas cell. However, we cannot control when the injection happens due to the random distribution of nanoparticles in the experiment. Combined control over how and where the electron injection happens could be achieved, for example, by using an aerodynamic lens.[23] However, developing and integrating such an aerodynamic lens into a gas target would require significant financial and human resources; thus, in this first instance, we focus only on the usefulness of nanoparticle-assisted wakefield acceleration.

II. EXPERIMENTAL METHOD

A. Overview

The experimental setup is shown in Fig. 1.

An f/50 spherical mirror focuses the intense petawatt-level laser pulses (135 fs pulse duration and 130 J energy) into a 10-cm-long gas cell filled with 99.9% purity helium and doped with aluminum nanoparticles. The leading edge of the laser pulse ionizes the gas, creating a plasma with an electron density of $6 \pm 0.5 \times 10^{17}$ cm^{-3}. Concurrently, the peak of the laser pulse excites an NPW in the bubble regime if the conditions are suitable to accelerate the electrons to high energy. The electron bunches from the LWFA are subsequently deflected by a 10-cm-long dipole magnet with a B-field of 0.79 T and detected on three scintillating screens 1.568, 2.556, and 5.855 m downstream of the exit pinhole of the gas cell. As detailed in Sec. IV, the use of multiple screens allows for cross-checking and an accurate reconstruction of the electron energy spectra independently of the initial pointing of the electron beam. The beam distribution spread measured on the screens includes components from the electron beam energy spread and the electron beam divergence. This beam divergence term thus limits the energy spread resolution of the electron spectrometer because it is not deconvolved due to the lack of simultaneous measurements of the electron beam divergence in the bend plane.

The farthest screen, DRZ3 (shown in Fig. 3), detects electrons with energies above 2 GeV, while the two closer screens, DRZ1 and DRZ2, detect electrons with energies above 0.4 GeV. As detailed in Sec. II D, we use an imaging plate and cross-correlation with the light emitted by the scintillating screens for charge calibration.

B. The Texas petawatt laser

The Texas Petawatt Laser delivers 130 ± 10 J pulses on target, with 45% of the total energy enclosed within $1/e^2$. The FWHM pulse duration is 135 ± 10 fs with a central wavelength of 1057 nm. An f/50 spherical mirror focuses the laser pulse at the entrance gas cell pinhole onto an FWHM focal spot of ~55 μm with a peak intensity of 1.2×10^{19} W/cm^2. The vacuum Rayleigh length is ~1.5 cm. The laser temporal contrast of the laser pulse, up to several tens of picoseconds before the main pulse peak, is on the order of 10^{-8}. The laser parameters are monitored before hitting the spherical mirror, and parameters including the energy, Strehl ratio, and collimation are

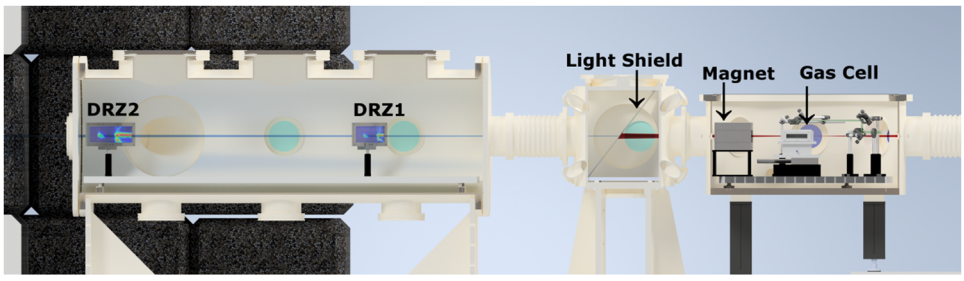

FIG. 1. The electron diagnostics setup, containing a gas cell, a dipole magnet, and two scintillating screens, DRZ1 and DRZ2. The entire setup is placed inside vacuum chambers. The laser and electron bunches propagate from right to left.

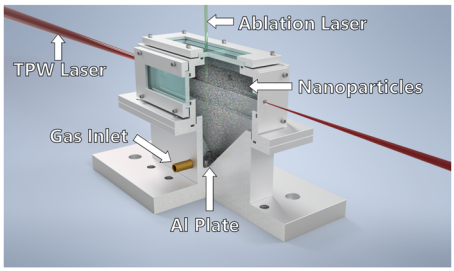

FIG. 2. A drawing of the gas cell. A 532-nm laser is focused through the top window onto the surface of a metal plate and generates the nanoparticles through laser ablation. The nanoparticles mix with the helium gas and fill the volume of the gas cell uniformly. The Texas Petawatt Laser enters the gas cell through a 3-mm-diameter pinhole and generates electrons that exit the gas cell through another 3-mm pinhole.

retrieved for each shot. More details on the TPW laser construction and performance can be found in the published literature.[24–26]

C. Gas target and nanoparticle source

A 3D drawing of the gas target[27] is shown in Fig. 2. Its design is based on the *SlitCell* design,[28] modified to accommodate a removable metal plate on the bottom of the gas cell for nanoparticle generation. The gas cell has two windows, one on the side and another on the top, which are used for laser alignment and visualization of the interaction region. The gas target is filled with helium via a solenoid valve opening for 2 ms with a delay of 27 ms before the main laser arrives. The gas density is monitored with a pressure transducer (with a measured standard deviation of 0.5 $\times$ 10^{17} cm^{-3}) installed in the middle of the gas cell wall. According to fluid dynamic simulations (not shown here), the gas density profile is uniform inside the gas cell and shows down-ramps outside the pinholes.

In shots with nanoparticles, an auxiliary laser pulse (532 nm wavelength, 10 ns pulse duration, and 130 mJ energy) is fired 500 μs prior to the main petawatt pulse onto an aluminum plate situated on the bottom of the gas cell near the gas inlet, ablating it and creating the nanoparticles.[29,30] Theoretical[21] and experimental[22] investigations have shown that the amount of charge injected into the bubble can be controlled by changing the nanoparticle's composition, size, or density. We used an aluminum plate for the work presented here, but most metals can be used as a solid plate or deposited on a support plate. The nanoparticles mixed with the helium gas to fill the gas cell uniformly. The ablation laser fluence was kept constant at 5 J/cm^2 for the entire experiment. We estimated using Ref. 30 that the mass of ablated aluminum per shot was m = 19 μg. For simplicity, we assume that the entire ablated mass was transformed into nanoparticles with a 10-nm diameter[22] uniformly distributed over the entire volume of the gas cell. In this case, ~10^6 to 10^7 nanoparticles could interact with the laser in a cylinder defined by the 50-μm laser spot diameter and the 10-cm gas cell length. While this provides a rough upper-bound estimate for the nanoparticle density, simplifying assumptions in this calculation lead us to believe that the actual nanoparticle density may be lower by a few orders of magnitude.

D. Electron beam diagnostics: Energy and charge

We deployed a multi-screen electron spectrometer[31] for the electron beam energy characterization, as shown in Fig. 3. This arrangement consists of a known static magnetic field and multiple scintillating screens to reconstruct the electron trajectories. It consists of a 0.79 T peak field dipole magnet between A and B and two DRZ1 and DRZ2 scintillating screens placed at C and D, respectively (imaged by two sCMOS cameras). Two Fuji BAS-SR imaging plates placed after the DRZ1 and DRZ2 screens were used for charge calibration of the scintillating screens. An imaging plate named DRZ3 placed at E in Fig. 3 detected electrons with energies higher than

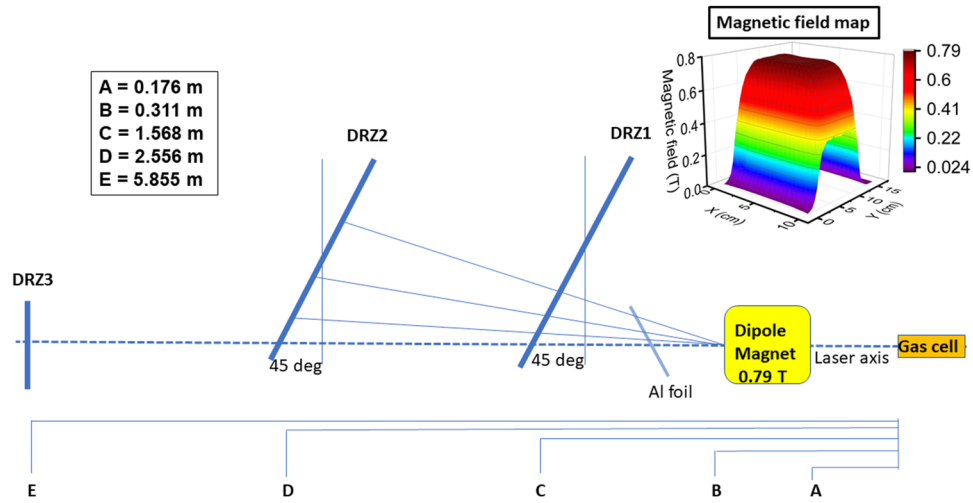

FIG. 3. A 2D drawing of the setup containing the gas cell and diagnostics. The inset shows the measured magnetic field map of the dipole magnet. The laser and electron bunches propagate from right to left.

2 GeV. The electron energy retrieving algorithm published by Hojbota *et al.*[32] was used to determine the energy spectrum of the electron beams produced in the laser wakefield experiment.

We employed the following analysis to mitigate the uncertainty generated by the electron beam angle and offset at the entry point of the dipole magnet.

An electron traveling through a magnetic field oriented perpendicular to its motion is subject to a Lorentz force:

$$\frac{d\mathbf{p}}{dt} = \frac{d}{dt}(\gamma m_e \mathbf{v}) = -e\mathbf{v} \times \mathbf{B}.$$

For simplicity, we will consider that the electron propagates solely in the $\hat{\boldsymbol{z}}$-direction initially before encountering the magnetic field and that the magnetic field is solely in the $\hat{\boldsymbol{y}}$-direction. Then, any deflection imparted onto the electron by the magnetic field is in the $\hat{\boldsymbol{x}}$-direction. We also assume that any radiation loss due to acceleration in the magnetic field is negligible compared to the electron's initial energy. Thus, we can approximate the effects of the magnetic field on the electron trajectory as

$$x(z) = \frac{v_x(z=0)}{v_z} z + \frac{e}{\gamma m_e v_z} \int_0^z dz' \int_0^{z'} dz'' B_y(z'').$$

For a relativistic electron, the propagation speed is nearly the speed of light, $v_z \approx c$. With this approximation, we can substitute in the electron energy $\epsilon = \gamma m_e c^2$ to obtain the following:

$$x(z) = \beta_{0x} z + \frac{ec}{\epsilon} \int_0^z dz' \int_0^{z'} dz'' B_y(z'').$$

The trajectory of the electron leaving the magnetic field can be determined by measuring the electron positions on two or more scintillating screens positioned after the magnet. The electron deflection is known, while the initial trajectory pointing is unknown. We can recover the energy of the electron by using the measured trajectory and propagating the electron backward through the detector system instead of forward propagating the electron from the source into the detector. In the backward propagation, this trajectory determines β_{0x} in the equation:

$$\beta_{0x} = -\frac{x_2 - x_1}{z_2 - z_1} = -\frac{\Delta x}{\Delta z}.$$

The energy of the electron producing the trajectory can be determined as

$$\epsilon = \frac{ec}{-x_2 + \frac{\Delta x}{\Delta z} z_2} \int_0^z dz' \int_0^{z'} dz'' B_y(z'').$$

One must also consider the errors in the measurement process. Consider some variation in the measured deflection δx_i. The impact on the energy can be determined as

$$\delta\epsilon_x = \left(\sum_i \left(\frac{\partial \epsilon}{\partial x_i}\right)^2 \delta x_i^2\right)^{1/2} = \epsilon\left(\left(\frac{-z_2 \delta x_1}{x_2 z_1 - x_1 z_2}\right)^2 + \left(\frac{z_1 \delta x_2}{x_2 z_1 - x_1 z_2}\right)^2\right)^{1/2},$$

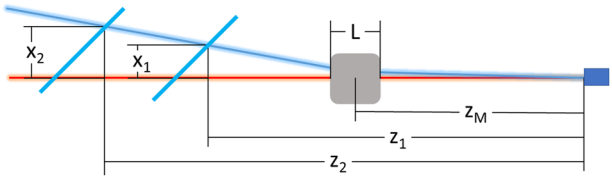

FIG. 4. A simplified setup used to calculate the error in the centroid electron energy. The laser and electron bunches propagate from right to left.

where the ith index corresponds to the ith scintillating screen (see Fig. 4).

For our design, $z_1 = 1.702$ m and $z_2 = 2.686$ m, as measured from the end of the gas cell to the intersection point on the scintillating screen. We expect variation in the measurement due to the optical system resolution being of the order of $\delta x_1 = 38\ \mu$m and $\delta x_2 = 60\ \mu$m. For a ~6 GeV electron energy, we expect $x_1 = 5.700$ mm and $x_2 = 9.765$ mm for the magnet used in this work. This results in $\delta\epsilon_x/\epsilon = 0.111$.

Similarly, we can estimate the variation in the energy measurement due to variations in the screen and magnet spacing. For simplicity, we will assume the true magnetic field can be approximated by a fixed field of strength B_0 over some length $L \pm \delta L$. Then, the energy of the electron is

$$\epsilon = \frac{ecB_0}{-x_2 + \frac{\Delta x}{\Delta z} z_2}\left(\left(z_2 - z_M + \frac{L}{2}\right)^2 - \left(z_2 - z_M - \frac{L}{2}\right)^2\right),$$

where $z_M \pm \delta z_M$ is the location of the center of the magnetic field. Note that the variation in the effective field strength corresponds to a minor variation in energy,

$$\frac{\delta\epsilon_B}{\epsilon} = \frac{\delta B}{B_0} = 0.0013,$$

for a field strength of $B_0 = 0.760$ T and $\delta B = 0.001$ T (with the latter an instrument measurement error). If we look at the variation in the propagation axis z, the variation in the energy can be quantified as

$$\frac{\delta\epsilon_z}{\epsilon} = \left(\left(\frac{z_2(x_1 - x_2)\delta z_1}{(z_2 - z_1)(x_2 z_1 - x_1 z_2)}\right)^2 + \frac{4(z_2 - z_M)^2 \delta L^2 + 4L^2 \delta z_M^2}{\left((z_2 - z_M + L/2)^2 - (z_2 - z_M - L/2)^2\right)^2} + \left(\frac{z_1(x_2 - x_1)}{(z_2 - z_1)(x_2 z_1 - x_1 z_2)} + \frac{2L}{(z_2 - z_M + L/2)^2 - (z_2 - z_M - L/2)^2}\right)^2 \delta z_2^2\right)^{1/2}.$$

For our spectrometer, the expected energy variation due to the positional location measurement error $\delta z_1 = \delta z_2 = \delta z_M = \delta L = 0.5$ mm is $\delta\epsilon_z/\epsilon = 0.009$ for a 6 GeV electron energy. The total error is given by

$$\frac{\delta\epsilon}{\epsilon} = \sqrt{\left(\frac{\delta\epsilon_x}{\epsilon}\right)^2 + \left(\frac{\delta\epsilon_z}{\epsilon}\right)^2} = 0.112.$$

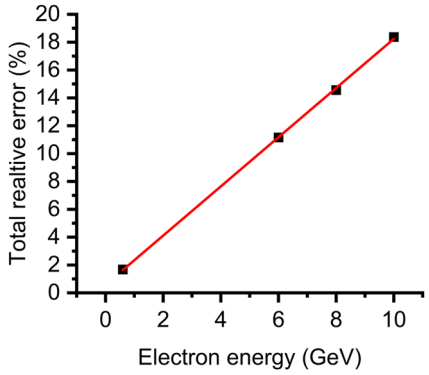

FIG. 5. The electron spectrometer total relative error in energy retrieval as a function of the electron energy.

At the lower energy limit of our spectrometer (~600 MeV), we expect electron trajectories with $x_1 = 54.660$ mm, $x_2 = 93.652$ mm, and $\delta x_1 = 41$ μm, $\delta x_2 = 63$ μm. The resolution is roughly the same as for the higher energy electron trajectories since we view the scintillating screen at a near-normal incidence. This yields $\delta\epsilon_x/\epsilon = \delta\epsilon_z/\epsilon = 0.012$. For low energies, we estimate the total error as $\delta\epsilon/\epsilon = 0.017$.

The total error energy as a function of the electron energy is shown in Fig. 5, where the maximum plotted error is 18.6% for a 10 GeV electron energy.

Using G4Beamlines,[33] a particle simulation and tracking program, we could simulate electron trajectories through our detector using various initial parameters while including the measured dipole field map. With these simulations, we could determine the parameter space (all the positions for all possible pointings between −1 and +5 mrad) for each detector scintillating screen (Fig. 6). For each experimental shot, we obtained the positions of the bunch or bunches on each screen, and using the parameter space diagrams, we determined which pointing corresponded to the same energy reading on both screens. This provided the energy calibration for plotting the shot and the spectrum. As a final check and when possible, the calibration was done for multiple points to ensure that different parts of the spectrum did not have different pointings.

Following calibration protocols found in the literature,[34–37] the imaging plates were used to cross-calibrate the electron beam charge impinging on the scintillating screens. The charge of the electron beam was determined from the imaging plate using the formula:

$$Q = \frac{Se}{R(E)\alpha(t,N)},$$

where S is the PSL signal from the imaging plate, e is the elementary charge, $R(E)$ is the imaging plate response sensitivity for a given incident electron energy E, and $\alpha(t,N)$ is the convoluted attenuation of the signal due to repeatedly scanning N times and the passage of time (t). Both $R(E)$ and $\alpha(t,N)$ were empirically determined.

To obtain the charges on the shots without an imaging plate, we correlated the charge obtained from the imaging plate with the light signal captured by our optical camera equipped with a narrow band-pass filter to remove some of the background light. All shots were taken with the camera set to zero gain and with a fixed exposure length. In an effort to avoid signal saturation of the CCD pixels, the aperture f-stop of the imaging lenses was set *a priori* based on our best estimate of the expected signal intensity. Each decrease in the aperture f-stop corresponds to a doubling of the light intensity on the sensor, and conversely, each increase in the aperture f-stop corresponds to a factor of two decrease in the light intensity. The f-stop for each shot was recorded, and the corresponding correction factor was applied to obtain the emission signal from the scintillating screen. As determined from shots recorded with the imaging plate signal, the scintillating screen emission signal showed a linear relationship with the electron beam charge. Despite our aim of avoiding the signal saturation regime, some electron spectra were saturated. The retrieved charge was underestimated in these cases.

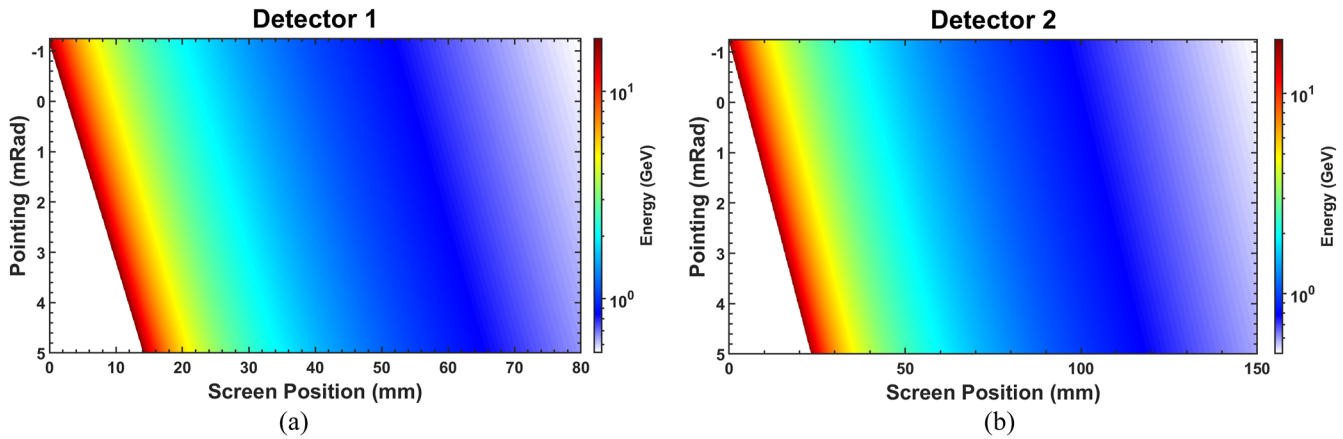

FIG. 6. The parameter space for the DRZ scintillating screens 1 and 2 (Detector 1 and Detector 2, respectively) for various initial electron pointings and energies. The experimental electron spectrum is matched on the two screens, and the corresponding pointings and energies are retrieved for each spectrum feature or each bunch.

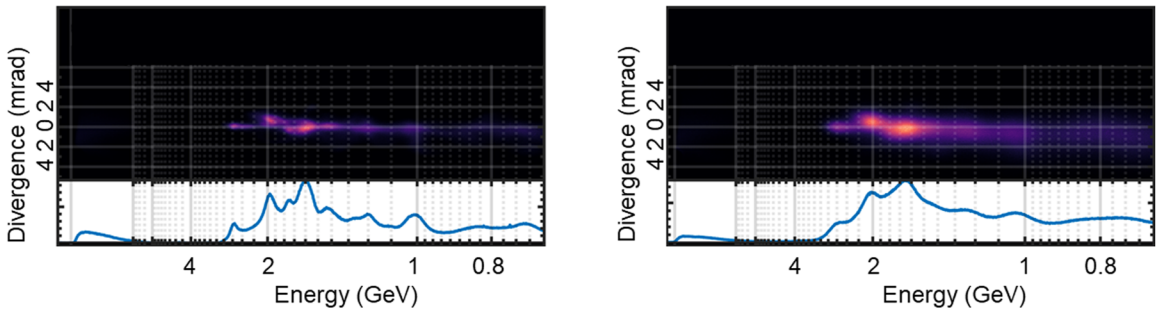

FIG. 7. A typical shot recorded without nanoparticles and shown on both DRZ screens. The difference in charge and divergence is due to the different responses of the DRZ screen and the optical system assembly.

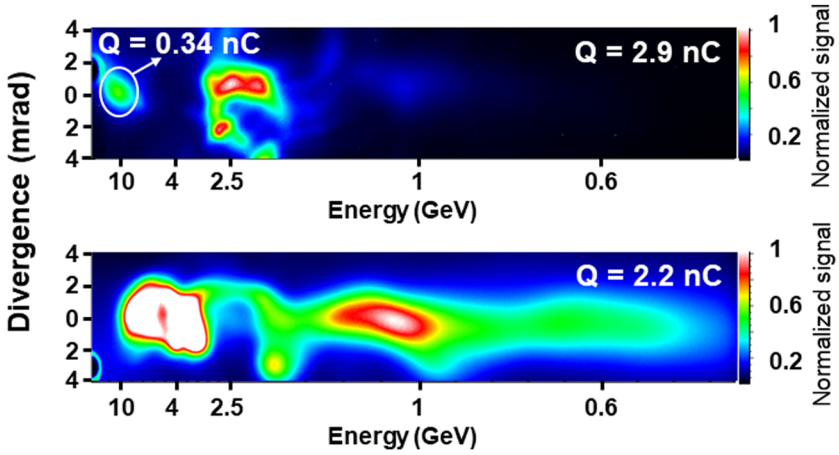

FIG. 8. Electron energy spectra of the two most energetic shots recorded by DRZ2. The energy spectra were recorded simultaneously on two consecutive screens to correct any off-axis electron beam pointing. The top spectrum shows a high energy bunch with the centroid at 10.4 ± 1.93 GeV, a 3.4 GeV rms energy spread, a 340 pC electric charge (2.9 nC total charge), and a 0.9 mrad rms divergence. The bottom energy spectrum shows a 4.9 ± 0.39 GeV centroid electron bunch with a tail energy that extends beyond 10.4 GeV and has a 2.2 nC total charge with a 1.4 mrad rms divergence. The energy spread from the electron beam divergence has not been deconvolved, and its value could be lower than estimated.

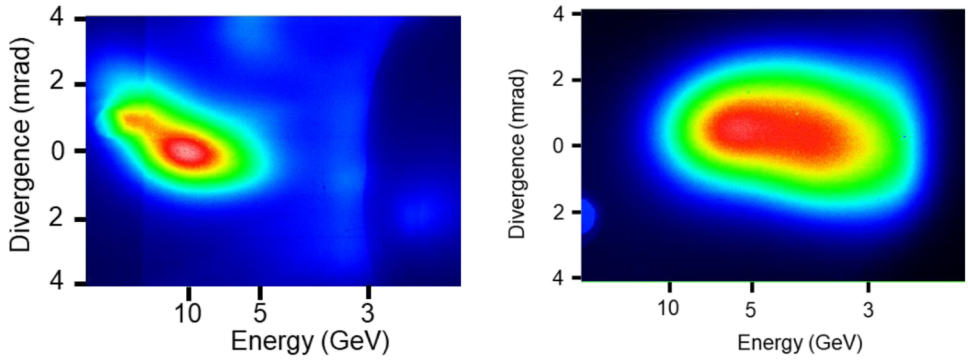

FIG. 9. Two of the most energetic electron spectra as viewed on DRZ3 (placed 5.855 m away from the exit of the gas cell) with an energy cutoff of ~2 GeV.

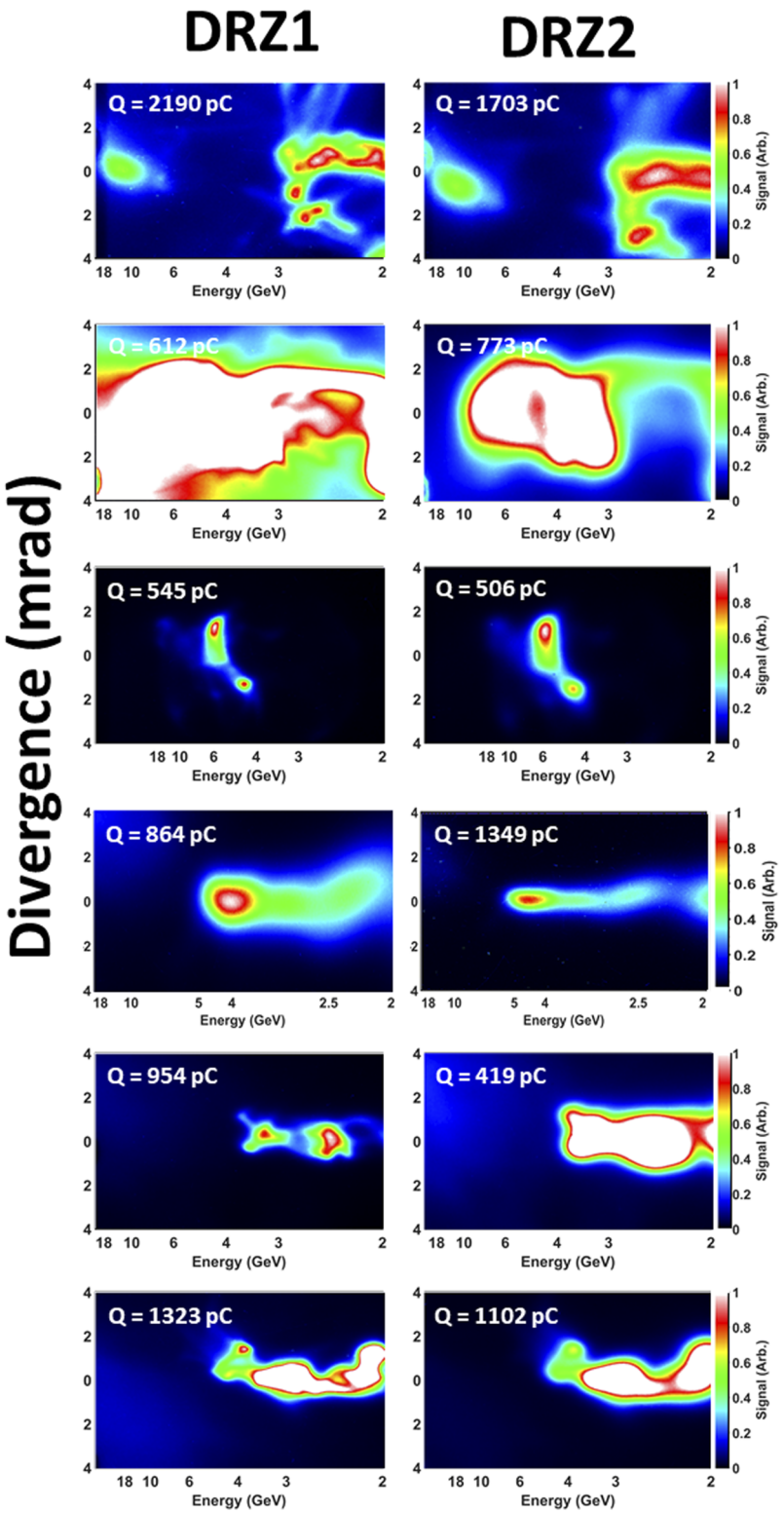

FIG. 10. Data showing the electron energy spectra with energies above 2 GeV recorded by DRZ1 (left column) and DRZ2 (right column). The DRZ1 screen was placed 1.568 m from the exit of the gas cell, and DRZ2 was placed at 2.556 m from the exit. The first two shots show the highest electron energies beyond 10 GeV.

TABLE I. The laser parameters corresponding to some of the highest electron energy shots. The electron energy is taken as the centroid of the highest energy bunch. The charge is taken from DRZ2 with a lower cutoff energy of 2 GeV.

Shot	Pulse duration (fs)	Laser energy (J)	Focal plane position (mm)	Strehl ratio	Electron centroid energy (GeV)	Total charge (pC)	Pointing correction (mrad)
1	134	118	7.21	0.72	10.40 ± 1.93	1703	0
2	143	125	7.05	0.4	4.90 ± 0.42	773	0
3	136	124	7.05	0.64	6.20 ± 0.68	506	2.2
4	147	97	4.21	0.58	4.50 ± 0.36	1349	0
5	139	128	7.69	0.61	3.50 ± 0.22	419	0
6	134	126	6.29	0.47	3.40 ± 0.20	1102	0.75

III. RESULTS

In baseline shots without nanoparticles, we produced typical electron bunches similar to those published by Wang *et al.*[38] with electron energies around 2 ± 0.08 GeV and charges of a few hundred pC (see Fig. 7).

The low repetition rate of the TPW laser precluded systematic parameter scans, and the nature of high-power laser systems with a limited beam time resulted in 26 successful shots (23 with and three without nanoparticles) in our experimental campaign, from which two shots with nanoparticles showed electron energies beyond 10.4 ± 1.93 GeV. The electron spectra that displayed the highest attained energies are shown in Figs. 8 and 9. Further electron spectra with energies beyond 2 GeV, including the already mentioned shots, with an energy lower bound cut at 2 GeV, are shown in Fig. 10 and summarized in Table I.

As an exemplification of the data analysis, let us consider shot number 3 (seen in Fig. 10 and Table I). The initial raw data exhibited two distinct electron bunches, and we accurately determined their positions on the DRZ screens. Subsequently, employing the analysis routine, we determined the unique solution that gave the pointing for each bunch while simultaneously displaying identical energy readings on both DRZ screens. Consequently, upon comparing the pointing values for each bunch, it was revealed that both exhibited identical values of 2.20 mrad (meaning that the electron energy was lower than the real one if uncorrected). Using this corrected pointing value, we derived the electron spectrum.

Similarly, the analysis conducted on shot number 6 necessitated a pointing correction of 0.75 mrad. In contrast, the remaining shots did not require any correction.

Although it is not obvious in Fig. 6 due to the limited optical resolution, the raw data used to generate the parameter space shows that within the experimental error, there is a unique solution that gives the same energy reading on both DRZ screens and has the same pointing.

The position of the laser focal plane was monitored during the experiment but was not accurately controlled and showed significant shot-to-shot fluctuations. We observed that the position of the focal plane inside the gas target was essential to controlling the electron energy, as noted in previous experiments with the TPW laser.[38] All electron energy spectra with peak energies beyond 3.5 GeV (all generated using nanoparticles) were obtained with the expected laser focal plane in vacuum (see Fig. 11) at 7 ± 1 mm inside the gas cell relative to the entrance pinhole.

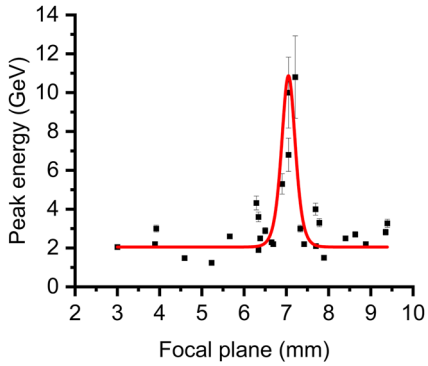

FIG. 11. The dependence of the maximum (or cut-off) electron energy on the position of the laser focal plane in the gas cell. It can be observed that all the shots with electron energies above 3.5 GeV are grouped around 7 ± 1 mm. The red curve is drawn to guide the eye, and the entrance pinhole is at 0 mm where the laser with a vacuum Rayleigh length of ~1.5 cm is focused.

The significant reliance of the outcome of the LWFA on the spatial location of the laser focal plane within the gas target may be attributed to the nonlinear evolution of the laser pulse and plasma wave being contingent upon the initial plasma conditions, as shown by Ciocarlan *et al.*[39] The potential impact of the entrance pinhole of the gas cell on the laser beam, which has not been quantified,[40] should also not be disregarded. Additional empirical and theoretical inquiries will be critical to elucidating the fundamental underlying mechanism, which is presently being actively investigated.

IV. DISCUSSION AND CONCLUSION

Currently, we do not have a satisfactory model or experimental explanation for the generation of such high electron energies. Various theoretical scenarios are now under investigation and, if relevant, will be the subject of future publications. Due to the prohibitive computational complexity and cost of performing a Particle-in-Cell (PIC) simulation in the full three-dimensional geometry of a 10-cm-long plasma with a known spatiotemporal shape laser pulse, and the additional need to resolve nanoparticles (with a resolution of

less than 5 nm), our future effort will focus on characterizing the nanoparticle-assisted wakefield accelerator in terms of the output electron parameters, i.e., by using better statistics and by probing the wakefields using few-cycle lasers[41] and electron beams.[42] Due to the high number of shots required for this experiment (statistics and probing), access to a high repetition rate petawatt-class laser (0.01–1 Hz) will be required.

In conclusion, we have shown in this nanoparticle-assisted laser wakefield acceleration experiment that we can produce electron bunches with high energies between 4 and 10 GeV. From the 26 recorded electron spectra under various experimental conditions, one electron spectrum showed an electron bunch with 0.34 nC of charge and a centroid energy of 10 ± 1.86 GeV, while another electron spectrum showed electron bunches with a tail extending beyond 10 GeV. Through further investigations using a high repetition PW-class laser, such as the ones found at *BELLA* at Lawrence Berkeley National Laboratory, *ALEPH* at Colorado State University, CoReLS in the Republic of Korea, or *ELI-NP* in Romania, we may be able to identify mechanisms to enable the production of 4–10 GeV electron beams and the experimental conditions required to improve their quality.

ACKNOWLEDGMENTS

B. M. Hegelich, C. Aniculaesei, T. Ha, L. Labun, O. Z. Labun, and E. McCary have been supported by the Air Force Office of Scientific Research Grant No. FA9550-17-1-0264. This work was supported by the DOE, Office of Science, Fusion Energy Sciences under Contract No. DE-SC0021125.

LaserNetUS: A Proposal to Advance North America's First High Intensity Laser Research Network. The contributions of A. Hannasch, R. Zgazdaj, I. Pagano, J. A. Franco, and M. C. Downer were supported by the U.S. Department of Energy Grant No. DE-SC0011617. D. A. Jarozynski, E. Brunetti, B. Ersfeld, and S. Yoffe would like to acknowledge support from the U.K. EPSRC (Grant Nos. EP/J018171/1 and EP/N028694/1) and the European Union's Horizon 2020 research and innovation program under Grant Agreement No. 871124 Laserlab-Europe and EuPRAXIA (Grant No. 653782). Simulation results were obtained using the ARCHIE-WeSt High-Performance Computer (www.archie-west.ac.uk) based at the University of Strathclyde, and the facilities of the N8 Centre of Excellence in Computationally Intensive Research (N8 CIR) provided and funded by the N8 research partnership and EPSRC (Grant No. EP/T022167/1), coordinated by the Universities of Durham, Manchester, and York.

Many thanks to Rémi Lehe of Lawrence Berkeley National Laboratory for his support in deploying and optimizing the FBPIC code.

AUTHOR DECLARATIONS

Conflict of Interest

Bjorn Manuel Hegelich and Constantin Aniculaesei submitted a patent application, 17/845,223, filled on June 21, 2021, describing the device and method to generate nanoparticles in a gas cell. B.M.H., L.L., O.Z.L., S.M., and M.E.D. are employed by the company Tau Systems, Inc., which is a company that develops and sells technology based on wakefield accelerators.

Author Contributions

C.A. and T.H. contributed equally to this work.

Constantin Aniculaesei: Conceptualization (equal); Data curation (equal); Formal analysis (equal); Investigation (equal); Methodology (equal); Writing – original draft (equal); Writing – review & editing (equal). **Thanh Ha**: Conceptualization (equal); Data curation (equal); Formal analysis (equal); Methodology (equal); Software (equal); Writing – original draft (equal); Writing – review & editing (equal). **Samuel Yoffe**: Investigation (equal); Writing – review & editing (equal). **Lance Labun**: Investigation (equal); Methodology (equal); Writing – review & editing (equal). **Stephen Milton**: Writing – review & editing (equal). **Edward McCary**: Investigation (equal); Methodology (equal); Writing – review & editing (equal). **Michael M. Spinks**: Investigation (equal). **Hernan J. Quevedo**: Investigation (equal); Writing – review & editing (equal). **Ou Z. Labun**: Writing – review & editing (equal). **Ritwik Sain**: Investigation (equal); Writing – review & editing (equal). **Andrea Hannasch**: Writing – review & editing (equal). **Rafal Zgadzaj**: Writing – review & editing (equal). **Isabella Pagano**: Writing – review & editing (equal). **Jose A. Franco-Altamirano**: Writing – review & editing (equal). **Martin L. Ringuette**: Resources (equal). **Erhart Gaul**: Resources (equal). **Scott V. Luedtke**: Writing – review & editing (equal). **Ganesh Tiwari**: Writing – review & editing (equal). **Bernhard Ersfeld**: Investigation (equal); Writing – review & editing (equal). **Enrico Brunetti**: Writing – review & editing (equal). **Hartmut Ruhl**: Writing – review & editing (equal). **Todd Ditmire**: Writing – review & editing (equal). **Sandra Bruce**: Writing – review & editing (equal). **Michael E. Donovan**: Writing – review & editing (equal). **Michael C. Downer**: Writing – review & editing (equal). **Dino A. Jaroszynski**: Writing – review & editing (equal). **Bjorn Manuel Hegelich**: Funding acquisition (equal); Investigation (equal); Project administration (equal); Supervision (equal); Validation (equal); Writing – review & editing (equal).

DATA AVAILABILITY

The data that support the findings of this study are available from the corresponding author upon reasonable request.

REFERENCES

[1] T. Tajima and J. M. Dawson, "Laser electron accelerator," Phys. Rev. Lett. **43**(4), 267–270 (1979).

[2] M. H. Key, "The *Physics of Laser Plasma Interactions*, W. L. Kruer. Addison-Wesley, 1988, £33.95, 182 pages.," J. Plasma Phys. **45**(1), 135 (1991).

[3] A. Pukhov and S. Gordienko, "Bubble regime of wake field acceleration: Similarity theory and optimal scalings," Philos. Trans. R. Soc., A **364**(1840), 623–633 (2006).

[4] W. Lu, C. Huang, M. Zhou, W. B. Mori, and T. Katsouleas, "Nonlinear theory for relativistic plasma wakefields in the blowout regime," Phys. Rev. Lett. **96**(16), 165002 (2006).

[5] F. Amiranoff *et al.*, "Observation of laser wakefield acceleration of electrons," Phys. Rev. Lett. **81**(5), 995–998 (1998).

[6]R. Wagner, S.-Y. Chen, A. Maksimchuk, and D. Umstadter, "Electron acceleration by a laser wakefield in a relativistically self-guided channel," Phys. Rev. Lett. **78**(16), 3125–3128 (1997).
[7]D. Strickland and G. Mourou, "Compression of amplified chirped optical pulses," Opt. Commun. **56**(3), 219–221 (1985).
[8]P. F. Moulton, "Spectroscopic and laser characteristics of Ti:Al_2O_3," J. Opt. Soc. Am. B **3**(1), 125 (1986).
[9]D. E. Spence, P. N. Kean, and W. Sibbett, "60-fsec pulse generation from a self-mode-locked Ti:sapphire laser," Opt. Lett. **16**(1), 42–44 (1991).
[10]J. Faure *et al.*, "A laser-plasma accelerator producing monoenergetic electron beams," Nature **431**(7008), 541–544 (2004).
[11]S. P. D. Mangles *et al.*, "Monoenergetic beams of relativistic electrons from intense laser-plasma interactions," Nature **431**(7008), 535–538 (2004).
[12]E. Brunetti *et al.*, "Low emittance, high brilliance relativistic electron beams from a laser-plasma accelerator," Phys. Rev. Lett. **105**(21), 215007 (2010).
[13]L. T. Ke *et al.*, "Near-GeV electron beams at a few per-mille level from a laser wakefield accelerator via density-tailored plasma," Phys. Rev. Lett. **126**(21), 214801 (2021).
[14]X. Wang *et al.*, "Petawatt-laser-driven wakefield acceleration of electrons to 2 GeV in 10^{17} cm^{-3} plasma," AIP Conf. Proc. **1507**, 341–344 (2012).
[15]A. J. Gonsalves *et al.*, "Petawatt laser guiding and electron beam acceleration to 8 GeV in a laser-heated capillary discharge waveguide," Phys. Rev. Lett. **122**(8), 084801 (2019).
[16]H. T. Kim *et al.*, "Enhancement of electron energy to the multi-GeV regime by a dual-stage laser-wakefield accelerator pumped by petawatt laser pulses," Phys. Rev. Lett. **111**(16), 165002 (2013).
[17]A. Pak, K. A. Marsh, S. F. Martins, W. Lu, W. B. Mori, and C. Joshi, "Injection and trapping of tunnel-ionized electrons into laser-produced wakes," Phys. Rev. Lett. **104**(2), 025003 (2010).
[18]K. Schmid *et al.*, "Density-transition based electron injector for laser driven wakefield accelerators," Phys. Rev. Spec. Top.–Accel. Beams **13**(9), 091301 (2010).
[19]C. Rechatin *et al.*, "Controlling the phase-space volume of injected electrons in a laser-plasma accelerator," Phys. Rev. Lett. **102**(16), 164801 (2009).
[20]B. Shen *et al.*, "Electron injection by a nanowire in the bubble regime," Phys. Plasmas **14**(5), 053115 (2007).
[21]M. H. Cho, V. B. Pathak, H. T. Kim, and C. H. Nam, "Controlled electron injection facilitated by nanoparticles for laser wakefield acceleration," Sci. Rep. **8**(1), 16924 (2018).
[22]C. Aniculaesei *et al.*, "Proof-of-principle experiment for nanoparticle-assisted laser wakefield electron acceleration," Phys. Rev. Appl. **12**(4), 044041 (2019).
[23]P. Liu, P. J. Ziemann, D. B. Kittelson, and P. H. McMurry, "Generating particle beams of controlled dimensions and divergence: II. Experimental evaluation of particle motion in aerodynamic lenses and nozzle expansions," Aerosol Sci. Technol. **22**(3), 314–324 (1995).
[24]E. W. Gaul *et al.*, "Demonstration of a 1.1 petawatt laser based on a hybrid optical parametric chirped pulse amplification/mixed Nd:glass amplifier," Appl. Opt. **49**(9), 1676–1681 (2010).
[25]E. Gaul *et al.*, "Improved pulse contrast on the Texas petawatt laser," J. Phys.: Conf. Ser. **717**(1), 012092 (2016).
[26]G. Tiwari *et al.*, "Beam distortion effects upon focusing an ultrashort petawatt laser pulse to greater than 10^{22} W/cm^2," Opt. Lett. **44**(11), 2764 (2019).
[27]B. M. Hegelich and C. Aniculaesei, "Particle-assisted wakefield electron acceleration devices," U.S. patent application 17/845,223 (2022).
[28]C. Aniculaesei, H. T. Kim, B. J. Yoo, K. H. Oh, and C. H. Nam, "Novel gas target for laser wakefield accelerators," Rev. Sci. Instrum. **89**(2), 025110 (2018).
[29]M. Kim, S. Osone, T. Kim, H. Higashi, and T. Seto, "Synthesis of nanoparticles by laser ablation: A review," KONA Powder Part. J. **34**, 80–90 (2017).
[30]K. H. Leitz, B. Redlingshöfer, Y. Reg, A. Otto, and M. Schmidt, "Metal ablation with short and ultrashort laser pulses," Phys. Procedia **12**(Part 2), 230–238 (2011).
[31]B. B. Pollock *et al.*, "Two-screen method for determining electron beam energy and deflection from laser wakefield," in *Proceedings of PAC09* (IEEE, 2009), pp. 3035–3037.
[32]C. I. Hojbota, H. T. Kim, J. H. Shin, C. Aniculaesei, B. S. Rao, and C. H. Nam, "Accurate single-shot measurement technique for the spectral distribution of GeV electron beams from a laser wakefield accelerator," AIP Adv. **9**(8), 085229 (2019).
[33]T. J. Roberts and D. M. Kaplan, "G4beamline simulation program for matter-dominated beamlines," in *Proceedings of the IEEE Particle Accelerator Conference* (IEEE, 2007), pp. 3468–3470.
[34]A. Buck *et al.*, "Absolute charge calibration of scintillating screens for relativistic electron detection," Rev. Sci. Instrum. **81**(3), 033301 (2010).
[35]K. Zeil *et al.*, "Absolute response of Fuji imaging plate detectors to picosecond-electron bunches," Rev. Sci. Instrum. **81**(1), 013307 (2010).
[36]J. P. Schwinkendorf *et al.*, "Charge calibration of DRZ scintillation phosphor screens," J. Instrum. **14**(09), P09025 (2019).
[37]Y. Glinec *et al.*, "Absolute calibration for a broad range single shot electron spectrometer," Rev. Sci. Instrum. **77**(10), 103301 (2006).
[38]X. Wang *et al.*, "Quasi-monoenergetic laser-plasma acceleration of electrons to 2 GeV," Nat. Commun. **4**, 1988 (2013).
[39]C. Ciocarlan *et al.*, "The role of the gas/plasma plume and self-focusing in a gas-filled capillary discharge waveguide for high-power laser-plasma applications," Phys. Plasmas **20**(9), 093108 (2013).
[40]N. Nakanii, K. Huang, K. Kondo, H. Kiriyama, and M. Kando, "Precise pointing control of high-energy electron beam from laser wakefield acceleration using an aperture," Appl. Phys. Express **16**(2), 026001 (2023).
[41]M. F. Gilljohann *et al.*, "Direct observation of plasma waves and dynamics induced by laser-accelerated electron beams," Phys. Rev. X **9**(1), 011046 (2019).
[42]Y. Wan *et al.*, "Direct observation of relativistic broken plasma waves," Nat. Phys. **18**(10), 1186–1190 (2022).
[43]C. Aniculaesei *et al.*, "Proof-of-principle experiment for nanoparticle-assisted laser wakefield electron acceleration," Phys. Rev. Appl. **12**(4), 044041 (2019).
[44]X. Wang *et al.*, "Quasi-monoenergetic laser-plasma acceleration of electrons to 2 GeV," Nat. Commun. **4**, 1988 (2013).